ADVANCED FUNCTIONAL MATERIALS
www.afm-journal.de

Minimal Surface-Based Materials for Topological Elastic Wave Guiding

Yuning Guo, Matheus Inguaggiato Nora Rosa, Mohit Gupta, Benjamin Emerson Dolan, Brandon Fields, Lorenzo Valdevit, and Massimo Ruzzene**

Materials based on minimal surface geometries have shown superior strength and stiffness at low densities, which makes them promising continuous-based material platforms for a variety of engineering applications. In this work, it is demonstrated how these mechanical properties can be complemented by dynamic functionalities resulting from robust topological guiding of elastic waves at interfaces that are incorporated into the considered material platforms. Starting from the definition of Schwarz P minimal surface, geometric parametrizations are introduced that break spatial symmetry by forming 1D dimerized and 2D hexagonal minimal surface-based materials. Breaking of spatial symmetries produces topologically non-trivial interfaces that support the localization of vibrational modes and the robust propagation of elastic waves along pre-defined paths. These dynamic properties are predicted through numerical simulations and are illustrated by performing vibration and wave propagation experiments on additively manufactured samples. The introduction of symmetry-breaking topological interfaces through parametrizations that modify the geometry of periodic minimal surfaces suggests a new strategy to supplement the load-bearing properties of this class of materials with novel dynamic functionalities.

1. Introduction

An ever-increasing quest exists for materials featuring low mass-volume ratios and high strength for applications that require superior structural, thermal, and acoustic performance.[1,2] For example, cellular materials have been extensively investigated due to their ability to tailor a broad range of material properties and to pursue multifunctionality.[3–6] In this context, minimal surfaces have emerged as promising platforms for continuous-based material designs.[2,7–11] Minimal surfaces are characterized by zero mean curvature and provide an efficient tessellation of space. These shell-based materials, also referred to in the literature as "shellular materials",[4,5,12] exhibit high stiffness and strength at ultralow densities,[4–6] and ensure lower sensitivity to stress concentrations with respect to truss-based cellular materials. The characteristics of minimal surfaces lead to materials with superior functionalities such as energy absorption, thermal management, and biomimetic designs, among others, which make them attractive solutions for applications in aerospace, civil, mechanical, and biomedical engineering.[5,6,9–11,13,14] While most prior investigations focus on static and strength properties, a few studies have been devoted to dynamic properties that leverage the periodic geometry of most minimal surfaces. These include for example the existence of frequency band gaps.[10,13,15] However, several dynamic functionalities remain unexplored, and significant opportunities exist to combine multiple advantageous static and dynamic mechanical properties within a single material platform. In this context, the recent explosion of activity in the field of topological metamaterials has uncovered numerous concepts for robust energy localization and defect-immune waveguiding. For example, the existence of robust interface modes in 1D periodic lattices has been demonstrated in references,[16,17] while elastic analogs of the Quantum Hall Effect,[18] Quantum Spin Hall effect,[19] and Quantum Valley Hall effect[20–23] have been established to induce backscattering immune waveguiding in 2D periodic elastic metamaterials. Additional studies have illustrated the existence of edge states and localized modes in quasiperiodic lattices,[24] and have explored the occurrence of higher-order topological modes and 3D topological phases in elastic systems.[25] These explorations mostly rely on demonstrator models[26,27] that, while effective at illustrating novel waveguiding properties, are not suitable for implementation within a continuous material platform. To this end, minimal surface geometries offer unexplored opportunities for the implementation of material concepts that integrate

Y. Guo, M. I. N. Rosa, M. Gupta, M. Ruzzene
P. M. Rady Department of Mechanical Engineering
University of Colorado Boulder
Boulder, CO 80309, USA
E-mail: massimo.ruzzene@colorado.edu
B. E. Dolan, L. Valdevit
Institute for Design and Manufacturing Innovation
University of California Irvine
Irvine, CA 92697, USA
E-mail: valdevit@uci.edu
B. Fields, L. Valdevit
Materials Science and Engineering Department
University of California Irvine
Irvine, CA 92697, USA
L. Valdevit
Mechanical and Aerospace Engineering Department
University of California Irvine
Irvine, CA 92697, USA
The ORCID identification number(s) for the author(s) of this article can be found under https://doi.org/10.1002/adfm.202204122.

DOI: 10.1002/adfm.202204122

efficient load-bearing capabilities and the ability to localize, guide, and steer elastic waves, which is relevant to applications related to noise isolation and absorption, vibration localization for energy harvesting and stress mitigation, among others.

Towards this goal, this paper investigates minimal surface-based metamaterials that support robust topological interface modes and waveguiding capabilities through the introduction of geometrical defects that break spatial symmetries to create topological interfaces. The topological phenomena of interest rely on the manipulation of symmetries that exist in minimal surfaces such as the Schwarz P surface.[10,28] Here, we modify the isosurface definition of the triply periodic Schwarz P surface to produce 1D and 2D dimerized assemblies that break cyclic C_2 and C_6 symmetries and feature topologically non-trivial band structures that produce edge states. Thus, in this work, we illustrate how topological defects can be introduced through simple geometrical parameterizations of minimal surface designs, which makes them suitable platforms for the implementations of waveguiding concepts based on non-trivial dispersion topologies within continuous material platforms. The results presented suggest that a variety of geometrical parameterizations can be engineered to manipulate wave motion in minimal surface-based metamaterials and to effectively pursue dynamic functionalities such as energy localization and waveguiding, with a potential for extension to 3D assemblies.

2. Geometry of Dimerized Minimal Surface-Based Materials

Minimal surfaces combine structure and material in an efficient manner by aligning force and geometry in an organic shape.[2,9,29] A minimal surface is defined by the points (x_1, x_2, x_3) that satisfy the iso-surface requirement $\phi(\boldsymbol{r}) = 0$, where $r = (x_1 i_1 + x_2 i_2 + x_3 i_3)$ denotes the position vector in space. As a starting point, we consider the triply periodic Schwarz P surface,[7] formed by the assembly of primitive cells depicted in **Figure 1**a (left), which illustrates its cubic symmetry. We generalize this geometry by introducing a set of reciprocal vectors, $\boldsymbol{b}_i$ $(i = 1, 2, 3)$ that enforce spatial periodicity. Accordingly, the surface is generally expressed as

$$\varphi(\boldsymbol{r}) = \sum_{n=1}^{N} f_n(\boldsymbol{b}_n \cdot \boldsymbol{r}) = 0 \tag{1}$$

where $N = 3$ and f_n are spatial functions, which for the case of Schwarz P surface are given by $f_n = \cos(\boldsymbol{b}_n \cdot \boldsymbol{r})$. Here $\boldsymbol{b}_n = \frac{2\pi}{a}\boldsymbol{i}_n$, where a is the lattice constant, while $\boldsymbol{i}_n$ $(n = 1, 2, 3)$ are the unit vectors associated with the cartesian frame of reference. This produces the cubic symmetric surface shown in the left panel of Figure 1a.

Inspired by the 1D Su–Schrieffer–Heeger (SSH) model,[30,31] we modify this baseline geometry by considering a surface dimerized along the x_1 direction, and limited to one unit cell in extent along the x_2, x_3 directions. This leads to the 1D structure of Figure 1c. To this end, we define f_1 as follows:

$$f_1(\boldsymbol{b}_1 \cdot \boldsymbol{r}) = \begin{cases} \cos\left(\dfrac{2}{1+\gamma}\boldsymbol{b}_1 \cdot \boldsymbol{r}\right), \text{for} -(1+\gamma)a \le \text{mod}(x_1, 2a) < 0 \\ \cos\left(\dfrac{2}{1-\gamma}\boldsymbol{b}_1 \cdot \boldsymbol{r}\right), \text{for} \; 0 \le \text{mod}(x_1, 2a) \le (1-\gamma)a \end{cases} \tag{2}$$

where $|\gamma| < 1$ is a stretching parameter that dimerizes the surface along x_1, while f_2, f_3 are kept unchanged. The expression in Equation (2) defines a stepwise modulation along x_1, which is described by the modulus "mod" operator, with $\boldsymbol{b}_1 = \frac{\pi}{a}\boldsymbol{i}_1$ being the new reciprocal lattice vector capturing the fact that the size of a unit cell is doubled along x_1 with a period of $2a$. Figure 1b shows the surfaces obtained for different γ. For $\gamma = 0$, one obtains the Schwarz P surface comprising two equal units of length a, while $\pm\gamma$ produces two distinct unit cells that are mirror-symmetric versions of each other, and that break the C_2 symmetry of the unit cell. We employ this parameterization to construct a 1D assembly along the x_1 direction, wherein two surfaces characterized by two equal and opposite $\pm\gamma$ values are joined (Figure 1c) to produce a topologically non-trivial interface of the kind investigated in references.[16,32] The corresponding physical test specimen shown in Figure 1c, whose close-up view is depicted in Figure 1d, is fabricated through Stereolithography using a photopolymer resin (formlabs durable resin 1L) (see Experimental Section).

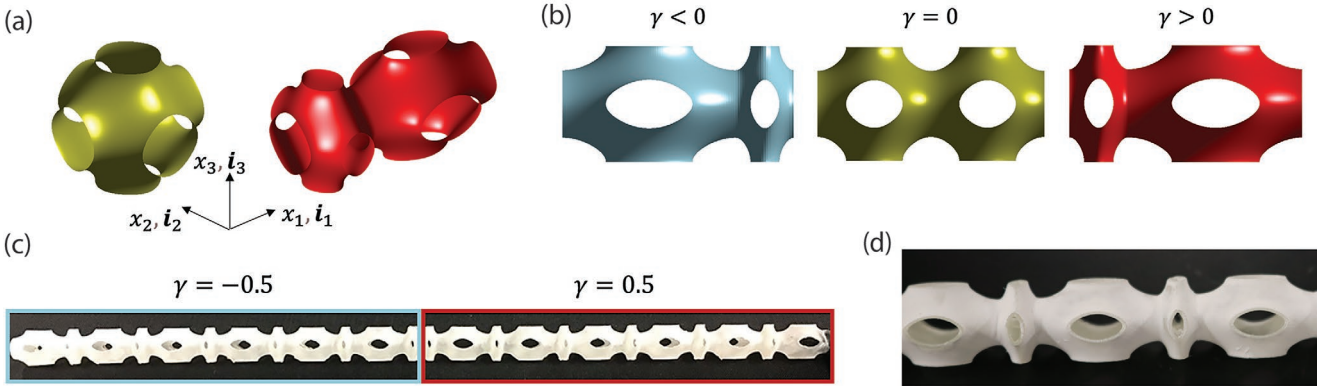

Figure 1. a) Unit cell of the Schwarz P surface, and dimerized version obtained for $\gamma \neq 0$ (see Equation (2)). b) Planar views of mirror-symmetric dimerized unit cells for $\gamma = 0$ (center) and $\pm\gamma$ (left and right). c) 1D dimerized assembly with non-trivial interface obtained by joining two surfaces corresponding to equal and opposite γ values, and d) close-up of fabricated sample employed in the experimental investigations.

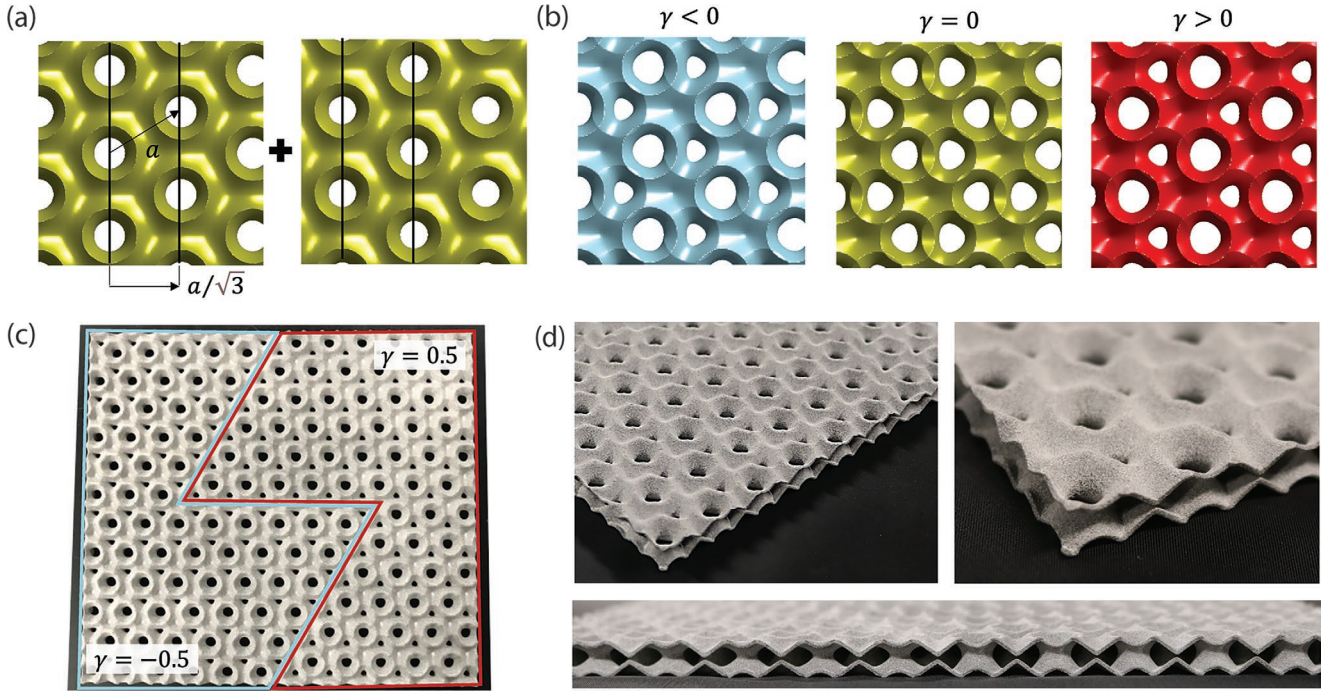

Figure 2. a) Planar view of the two C_6 symmetric surfaces that are translated relative to each other a quantity $\boldsymbol{r}_S = \frac{a}{\sqrt{3}}\boldsymbol{i}_1$. b) Their superposition based on weighted relative amplitude defined by γ leads to C_{3v} symmetric surfaces. c) 2D hexagonal assembly with an interface obtained by joining surfaces characterized by equal and opposite $\pm\gamma$ values along the highlighted path. d) Perspective view of the sample used for experimental testing, which shows the limited extension of the 2D assembly in the out-of-plane direction.

Next, we form a 2D hexagonal surface which is also dimerized to break C_6 symmetry in the x_1,x_2 plane, while retaining C_{3v} symmetry. Following the approach in references,[21,22,26] symmetry breaking produces distinct degrees of freedom at opposite valleys corresponding to high symmetry points in reciprocal space whereby wave functions feature opposite polarizations and thus emulate spin-orbit interactions.[33] The parameterization considers a hexagonal surface which is formed by the superposition of two triangular tessellations that are translated relative to each other by a quantity $\boldsymbol{r}_S = \frac{a}{\sqrt{3}}\boldsymbol{i}_1$ (**Figure 2**a). Their relative amplitude is modulated by a parameter γ, with the case of $\gamma = 0$ yielding to the 6-fold (C_6) symmetric surface, while $\pm\gamma$ values produce the distinct dimerized surfaces shown in Figure 2b. These are constructed by expressing f_1 and f_2 in Equation (1) as

$$f_1 = \frac{(1-\gamma)}{3}\left|\cos\left(\boldsymbol{b}_1\cdot\boldsymbol{r}\right)+\cos\left(\boldsymbol{b}_2\cdot\boldsymbol{r}\right)+\cos\left(\left(\boldsymbol{b}_1+\boldsymbol{b}_2\right)\cdot\boldsymbol{r}\right)\right| \quad (3)$$

$$f_2 = \frac{(1+\gamma)}{3}\left|\cos\left(\boldsymbol{b}_1\cdot\boldsymbol{r}'\right)+\cos\left(\boldsymbol{b}_2\cdot\boldsymbol{r}'\right)+\cos\left(\left(\boldsymbol{b}_1+\boldsymbol{b}_2\right)\cdot\boldsymbol{r}'\right)\right| \quad (4)$$

with $\boldsymbol{r}' = \boldsymbol{r} - \boldsymbol{r}_S$, while $\boldsymbol{b}_1 = \frac{2\pi}{a}\left(\frac{1}{2}\boldsymbol{i}_1 + \frac{\sqrt{3}}{2}\boldsymbol{i}_2\right)$, $\boldsymbol{b}_2 = \frac{2\pi}{a}\left(\frac{1}{2}\boldsymbol{i}_1 - \frac{\sqrt{3}}{2}\boldsymbol{i}_2\right)$ are the reciprocal lattice vectors in the x_1, x_2 plane. In the definition of the tessellation developing in the x_1, x_2 plane, f_3 and $\boldsymbol{b}_3$ are kept the same as introduced below Equation (1). The expression of f_1 considers the superposition of three cosines aligned along directions separated by 60°, which defines a modulation with triangular symmetry. Hence, considering only f_1 and f_3 produces the triangular surface of Figure 2a, while employing the superposition of f_2 and f_3 produces the same surface translated by $\boldsymbol{r}_S$. Finally, the superposition of the three functions f_1, f_2, f_3 leads to a hexagonal surface when $\gamma = 0$, and dimerized hexagonal surfaces with $\gamma \neq 0$ (Figure 2b). We employ this parameterization to construct a 2D dimerized surface in the x_1,x_2 plane, with x_3 limited within [0, a]. Following the approach of the 1D case, we form an interface joining surfaces characterized by two equal and opposite γ values along a predefined path. This leads to a topologically non-trivial interface of the kind investigated in references[21–23] and shown in Figure 2c. Figure 2d shows perspective views of the fabricated 2D sample, which is fabricated in Nylon 12 (HP 3D High Reusability PA 12) through Multi-Jet Fusion using an HP 4200 3D printing machine (see Experimental Section).

The surfaces illustrated above are inspired by the Schwarz P minimal surface, where desired symmetries and topological interfaces are incorporated into the surface definition. We note that the dimerized surfaces are no longer rigorously minimal surfaces given the fact that their mean curvature deviates from zero, which is the condition satisfied for example by the Schwarz P surface and by other similar geometries. The analysis of the mean curvature for the considered dimerized surfaces is in the Supporting Information for completion of the description of the proposed designs.

3. Results

We investigate wave propagation properties of the considered minimal surface-based materials through numerical

simulations and experiments. The models are formulated within the COMSOL environment, where dispersion spectra are computed to highlight the presence of band gaps and to evaluate their topological properties in the reciprocal space. Simulations on finite domains illustrate the existence of interface modes, which is confirmed by experiments conducted on the additively manufactured samples.

3.1. 1D Dimerized Minimal Surface-Based Material

The 1D dimerized surfaces of Figure 1 have a lattice constant of $2a = 15$ mm and a wall thickness of 0.5 mm. In the numerical simulations, we consider the nominal properties of the resin, namely Young's modulus $E = 1.77$ GPa, Poisson's ratio $\nu = 0.35$, and density $\rho = 1100$ kg m^{-3} (see Experimental Section). **Figure 3**a,b shows the band structures of unit cells with $\gamma = 0$ and $\gamma = \pm 0.5$, respectively, where we identify a pair of flexural bands (blue dots), which are degenerate due to the symmetry of the structure cross-section, one longitudinal band (red dots), one torsional band (black dots), and hybridized bands (green dots). The color-coding of the branches is based on the computation of a polarization coefficient that tracks the polarization of the modes and that is computed according to the procedure described in the Supporting Information (see Equations S2–S4, Supporting Information). To demonstrate the distinct vibration modes of the 1D dimerized surface, three representative mode shapes of the flexural, longitudinal, and torsional branches are displayed in Figure 3c (video animations are provided in the Supporting Information).

In Figure 3a, we note that the double periodicity of the unit cell along the x_1 direction for $\gamma = 0$ causes folding of the bands, which forms degeneracies at the edges of the Brillouin zone. These degeneracies are lifted upon breaking the inversion symmetry of the unit cell for $\gamma \neq 0$, which opens band gaps. The case for the dimerized cell with $\gamma = \pm 0.5$ is illustrated in Figure 3b, where the three band gaps are highlighted by shaded colored areas, corresponding flexural (blue), longitudinal (red), and torsional (black) modes. In addition to the parameter γ, the formed bandgaps depend upon the material properties (Young's modulus, density) and geometry of the structure (unit cell dimensions, wall thickness). The variation of these gaps as a function of selected material and geometrical parameters is presented in the Supporting Information for completeness. The evolution of the gaps as a function of the dimerization parameter γ is illustrated in Figure 3d, which shows the occurrence of a band inversion characterized by the gaps closing and re-opening as γ crosses zero and changes sign. This band inversion is associated with a change in the topology of the bands, which is characterized by the computation of the Zak phase as the relevant topological invariant.[34] The calculation procedure of the Zak phase, which has been reported in several prior

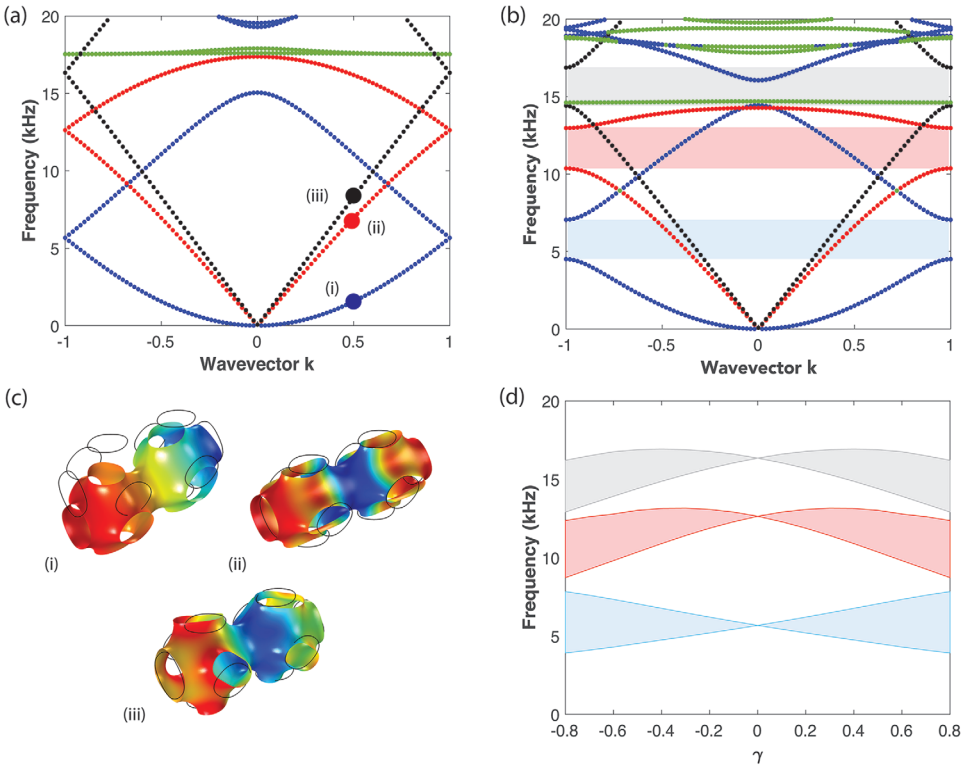

Figure 3. a) Band structures of 1D dimerized surface with $\gamma = 0$. The flexural, longitudinal, and torsional bands are respectively identified by blue, red, and black dots, while hybrid modes are denoted by green dots. This color-coding is defined by the value of the polarization coefficients computed for each branch. b) Band structures of 1D dimerized surface with $\gamma = \pm 0.5$. The gaps are highlighted by shaded areas whose color matches that of the bands it separates. c) Representative modes of the flexural, longitudinal, and torsional branches in 1D dimerized surface with $\gamma = 0$, respectively. The modes are computed for $k = 0.5$ at the points highlighted by colored circles in (a). d) Evolution of the gaps as a function of the stretching parameter γ, showing the band gaps closing and re-opening following a band inversion caused by geometrical inversion of the unit cell.

studies, is described in the Supporting Information. Herein, we treat bands of different polarizations independently, and we compute associated topological gap labels by considering only the bands of equal polarization. For example, the gap label for the longitudinal gap (red gap in Figure 3b) is obtained by summing the Zak phase of only the longitudinal bands below it. It is noted that the Zak phase of each dimerized cell is a gauge-dependent value that depends on the choice of the origin of the unit cell, while the difference between the Zak phases for the two configurations are equal to π if they are topologically distinct.[30] The difference of the Zak phases between the $\gamma = 0.5$ and the $\gamma = -0.5$ configurations are estimated as π for the degenerate flexural bands, longitudinal band, and torsional band below their corresponding bandgaps. Thus, the band gaps of the unit cells with $\gamma = \pm 0.5$ are associated with different topological invariants, and their phases are topologically distinct in spite of their identical band structures. This topological distinction is exploited for the design of the waveguide with the non-trivial interface of Figure 1c, which separates 6 cells with $\gamma = -0.5$ from 6 cells with $\gamma = +0.5$.

The eigenfrequencies of this finite system are computed and displayed in **Figure 4**a, where they are organized according to the polarization of the corresponding eigenstates, adopting the same color code used in Figure 3. The gaps are also highlighted as shaded areas of corresponding colors. Notably, localized states highlighted by cyan circles appear inside each of the band gaps due to the non-trivial interface. The associated mode shapes are displayed in Figure 4b, which confirm their localized nature at the interface and their polarization at 6.34, 11.41, and 16.67 kHz, respectively (see Supporting Information for animations of the interface modes).

Experiments on the additively manufactured sample of Figure 1c,d confirm the existence of the flexural interface mode. In the tests, the waveguide is mounted to an electrodynamic shaker which excites its transverse motion (perpendicular to the x_1 axis). The velocities of the points belonging to a grid aligned along the axis of the specimen are recorded by a Scanning Laser Doppler Vibrometer (SLDV). The shaker is mounted slightly to the left of the interface in order to induce the anti-symmetric flexural mode denoted as (i) in Figure 4b. The structure is excited by a broadband chirp signal excitation in the range of 3–10 kHz, within which a response transmission coefficient $T(x_1,\omega)$ is computed as the ratio of the response at location x_1 to the response at the excitation point ($x_1 = 0$). The excitation of the asymmetric mode of interest is enhanced through linear superposition by averaging the transmission response at mirror-symmetric points, that is, $T_{av}(x_1) = (T(x_1,\omega) - T(-x_1,\omega))/2$. This process reproduces the case where the 1D dimerized surface is simultaneously excited by two out-of-phase sources placed at mirror-symmetric locations across the interface, thus mimicking a dipolar excitation. The resulting transmission results are displayed in Figure 4c, where the red line

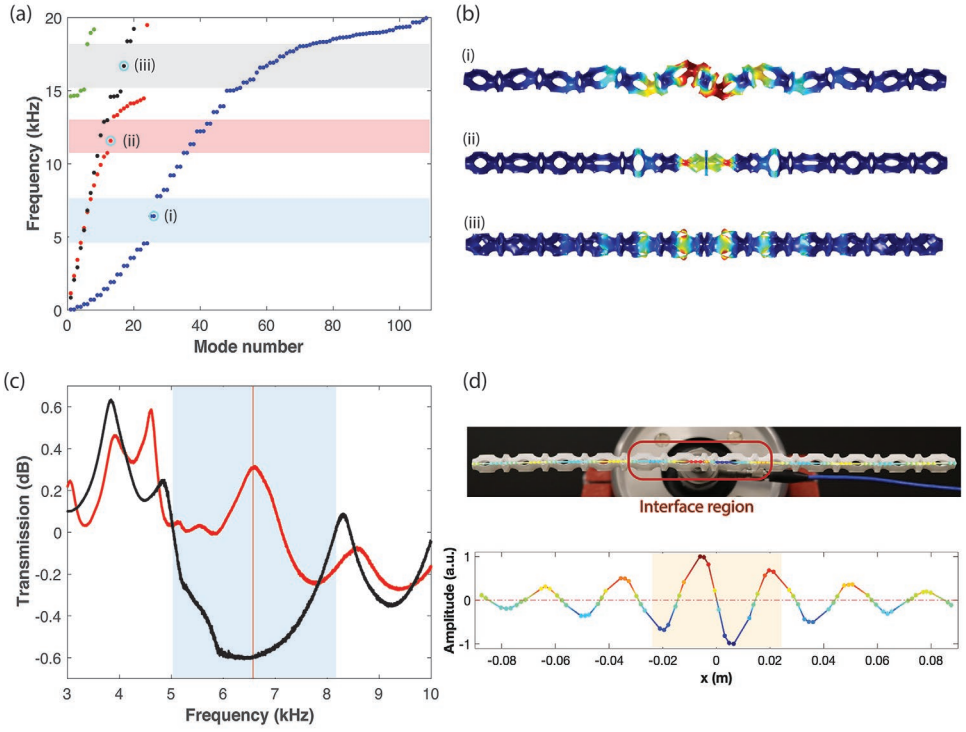

Figure 4. a) Eigenfrequencies of the 1D dimerized waveguide of Figure 1d: the three gaps are highlighted by the color code used in Figure 3; interface modes for flexural (i), longitudinal (ii), and torsional (iii) polarizations populate the 3 gaps and are highlighted by the cyan circles. b) Flexural (i), longitudinal (ii), and torsional (iii) interface modes at 6.34, 11.41, and 16.67 kHz, respectively. The color corresponds to the normalized displacement magnitude, varying from blue (minimum) to red (maximum). c) Experimentally measured transmission averaged across the interface (red) over the remaining length of the waveguide (black). The experimental flexural band gap is highlighted by the shaded blue region. The interface transmission (red) features a peak inside the gap that corresponds to the interface mode shown in (d). d) Experimental set-up and measured interface mode at 6.57 kHz: the transverse motion is excited by an electrodynamic shaker and it is recorded by a SLDV.

corresponds to the transmission averaged within the region of the interface (highlighted in the upper panel of Figure 4d), while the black line corresponds to the transmission averaged over the remaining length. The red curve evidences the presence of a transmission peak at 6.57 kHz, which occurs inside the flexural bandgap (shaded blue region in Figure 4c). Figure 4d shows the experimental set-up and the measured interface mode at 6.57 kHz, confirms the localized and asymmetric nature of the mode, and shows a general agreement with the numerical predictions for the interface mode of Figure 4b. The flexural mode can also be excited when the shaker is mounted at the end of the surface. Corresponding experimental results are provided in the Supporting Information, and show a similar localization pattern for this mode. The measurements are conducted using a single beam laser vibrometer, which primarily detects the displacement component perpendicular to the structure, and does not detect longitudinal and torsional motion in a straightforward way. These mode polarizations might be measured by exploiting more complex measurement set-ups, which leverage lateral contractions or differential displacements at given axial locations. The additional complexity in measurement may not add significantly in terms of illustrating the onset of localized modes, which is confirmed for the transverse mode. Numerical evidence of the existence of these modes is included in the Supporting Information.

3.2. 2D Hexagonal Minimal Surface-Based Material

The 2D hexagonal surface described by Equations (3) and (4) is investigated next. The lattice constant a is 17.4 mm and the wall thickness of the shell is 0.8 mm. The elastic properties of the base material ($E = 1.5$ GPa, $\nu = 0.40$) are measured by dynamic mechanical analysis (DMA) and through quasi-static mechanical testing, while the material density, $\rho = 1028$ kg m^{-3}, was measured through an Archimedes setup (see Supporting Information for details of the employed material characterization procedures).

The band structure for the unit cell of the 2D hexagonal surface in Figure 2 is presented in **Figure 5**a, which only shows the dispersion branches corresponding to the out-of-plane polarization, extracted on the basis of the corresponding polarization coefficient. This polarization is chosen due to its relevance to the experimental measurements. A notable feature of the band structure of Figure 5a is the symmetry of the branches, which reflects the C_6 symmetry of the 2D periodic surface, and the presence of Dirac cones at the high symmetry valley points K and K' of the Brillouin zone. The C_6 symmetry is broken to produce a surface characterized by C_{3v} symmetry for $\gamma \neq 0$. The band diagram for $\gamma = 0.5$ shown in Figure 5b features band gaps that are opened by breaking symmetries, which lifts the Dirac cone degeneracy. While the branches still appear symmetric about the Γ point, they are characterized by distinct topological phases at the valleys (K and K'), which is also the result of the broken spatial inversion symmetry. The distinct topology at the valley points is evidenced by the nonzero valley Chern numbers of opposite signs at K_1 and $K_1^{'}$ (details on the computation of valley Chern numbers as topological invariants are provided in the Supporting Information).[17,21] The chirality of the valley modes associated with their pseudospin is illustrated by the animations provided in the Supporting Information, which further confirms their opposite topological character. This identified distinction is leveraged to introduce a topological interface by combining surfaces characterized by two topologically distinct phases which are induced by opposite values of γ. For instance, the valley at K exhibits a clockwise pseudospin for the $\gamma = 0.5$ case, and a counterclockwise pseudospin for the $\gamma = -0.5$ case.

A 2D hexagonal surface material with an interface is constructed by joining 2D dimerized surfaces with opposite γ values ($\pm$ 0.5). An eigenvalue computation is performed for a finite strip that includes 18 cells aligned along the x_1 direction, 9 of which are characterized by $\gamma = -0.5$, while the remaining 9 cells by $\gamma = +0.5$. Imposing free boundary conditions at the edges along the x_1 direction, and periodic Bloch boundary conditions along the boundaries aligned with the x_2 direction produces the finite strip dispersion diagram in Figure 5c, which reveals the presence of an interface mode inside the gap.

Finally, a zigzag domain wall aligned with the lattice vectors is introduced to separate the two distinct phases defined by opposite γ values (Figure 2c), and to evaluate the ability to confine wave motion along this non-trivial interface. To this end, the harmonic response of the 2D surface with the interface is computed for excitation at the frequency corresponding to the interface mode of Figure 5c (6.89 kHz). Excitation at the midpoint of the surface produces the harmonic response shown in Figure 5d, which confirms the confinement of motion along the predefined zig-zag interface. We note that the observed motion is the result of the propagation of an elastic wave that is capable of managing a 120° sharp turn, without being reflected, which is one of the hallmarks of topologically protected wave motion.[23]

Vibration experiments are conducted on the additively manufactured surfaces shown in Figure 2c. As in the 1D experiments, an electrodynamic shaker is attached at the center of the sample to induce transverse vibrations (along x_3). First, transient tests are conducted to experimentally evaluate dispersion properties by applying broadband excitation within the frequency range of interest. The wavefields $w(x_1,x_2,t)$ recorded by the SLDV over a 2D grid are processed via 3D Fourier transformation (3D FT), resulting in their reciprocal space representation $\hat{w}(k_1,k_2,\omega)$, which maps the amplitude content of the wavefield in the frequency/wavenumber domain.[26,35] Here, a broad-band 2-cycle sinusoidal burst of center frequency of 8 kHz is applied to surfaces characterized by $\gamma = 0$ and $\gamma = 0.5$ (without an interface). The magnitude of the resulting spectral contents $|\hat{w}(k_1,k_2,\omega)|$ is plotted in the form of colormaps that are superimposed to the numerical dispersion curves (dotted lines) in **Figure 6**a,b. An overall agreement with the out-of-plane modes is observed, along with the confirmation of the presence of the Dirac points for $\gamma = 0$, and the opening of the gap for $\gamma = 0.5$. A small portion of the energy is observed to leak into additional modes in the figure (red dots), which are predominantly in-plane modes that were excluded from the plots of Figure 5 which showed only out-of-plane modes. Next, we employed narrow-band 36-cycle harmonic signals to illustrate the wavefields behavior at selected frequencies. Figure 6c shows a snapshot of the transient wavefield at 3.09 ms for the $\gamma = 0$ case for a center frequency

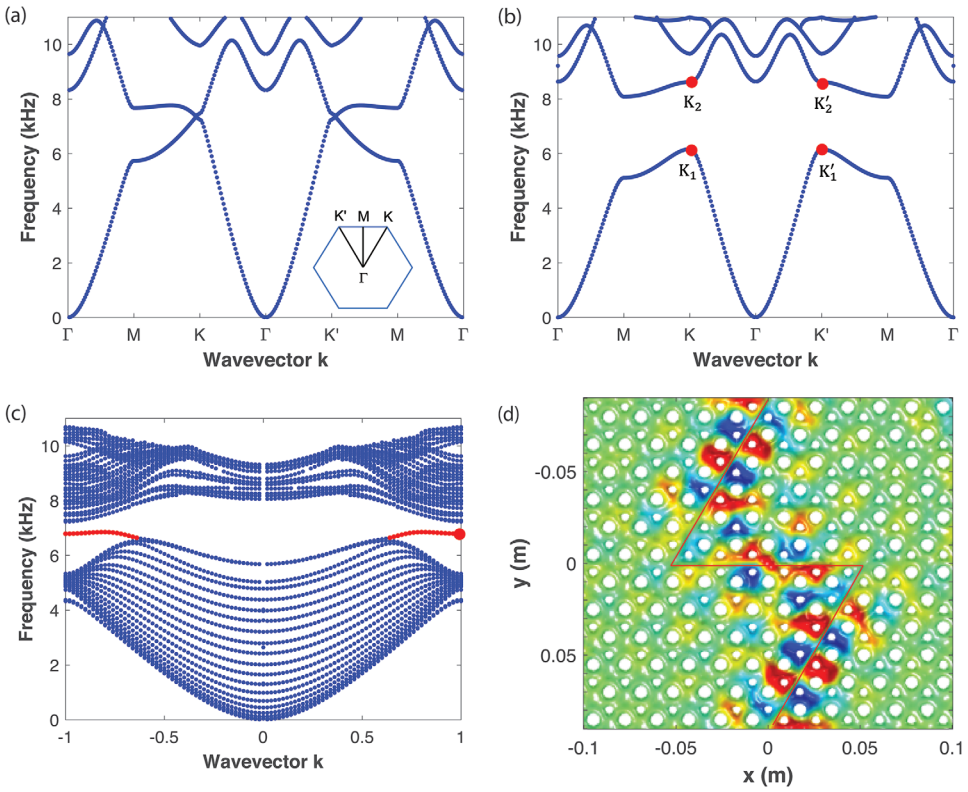

Figure 5. a) The band structure of the 2D hexagonal surface with $\gamma = 0$ features Dirac points at the high-symmetry valley points *K* and *K'*. The inset illustrates the reduced Brillouin zone. b) Band structure of the 2D hexagonal surface with $\gamma = 0.5$ showing opened band gaps resulting from broken symmetries. c) Band structure of the finite strip including the non-trivial interface obtained by joining two semi-finite hexagonal surfaces with opposite γ values ($\gamma = \pm 0.5$). d) Harmonic response of the plate at 6.89 kHz, which corresponds to one edge state marked in (c), illustrating wave motion confinement along the zigzag non-trivial interface.

of 8 kHz, which is chosen to be close to the Dirac point. The wavefield shows evidence of the 6-fold symmetric nature of the wavefront corresponding to the C_6 symmetry of the 2D hexagonal surface. In contrast, the wavefield of the surface comprising of $\gamma = \pm 0.5$ with an interface is recorded at a center frequency of 6.75 kHz, which is a frequency inside the band gap. The snapshot at 4.30 ms in Figure 6d demonstrates the confinement of the wave motion along the zigzag interface and highlights how the wave can perform a sharp turn with minimal backward reflection (See Supporting Videos for animations that clearly show waveguiding over time).

4. Conclusions

In conclusion, we have reported the geometrical parameterization of minimal surfaces and demonstrated their functionality as topological mechanical metamaterials. The considered 1D and 2D dimerized surfaces modify the primitive structure of the Schwarz P surface to introduce topologically non-trivial interfaces. The geometric parametrizations employed produce distinct topological phases that are created through selective breaking of spatial inversion symmetries to form topological interfaces within the continuous material framework of minimal surfaces. The considered interfaces show the ability to support localized modes in the 1D case, and wave confinement along a zig-zag interface that separates two distinct phases in the 2D case. The results presented suggest that the geometric modifications considered can naturally be employed at different length scales and operate at different ranges of frequencies upon proper scaling of the considered geometries.

These investigations contribute to the advancement of fundamental knowledge and new concepts for topological metamaterials. The results suggest a suitable material platform within which topological concepts can be introduced to complement other advantageous mechanical properties as in the case of minimal surface-based structures. The proposed configurations also suggest other avenues whereby configurations could be engineered to induce a variety of complex wave phenomena, and to extend them to 3D assemblies. These include for example topological channels or quasiperiodic modulations providing rich wave localization capabilities. In addition, the geometry of the considered class of minimal surface-based materials could be adapted to target properties, structural configurations, choice of constituent materials, length scales, and manufacturing processes to pursue a wide range of engineering applications at different spatial scales, from structural components, to nano or micro-electromechanical devices. Other potential areas of future studies include active configurations,[36] which in the context of shell-based materials may enable the time reconfiguration and activation of topological interfaces by inducing geometrical changes, primarily in the form of curvature. Moreover,

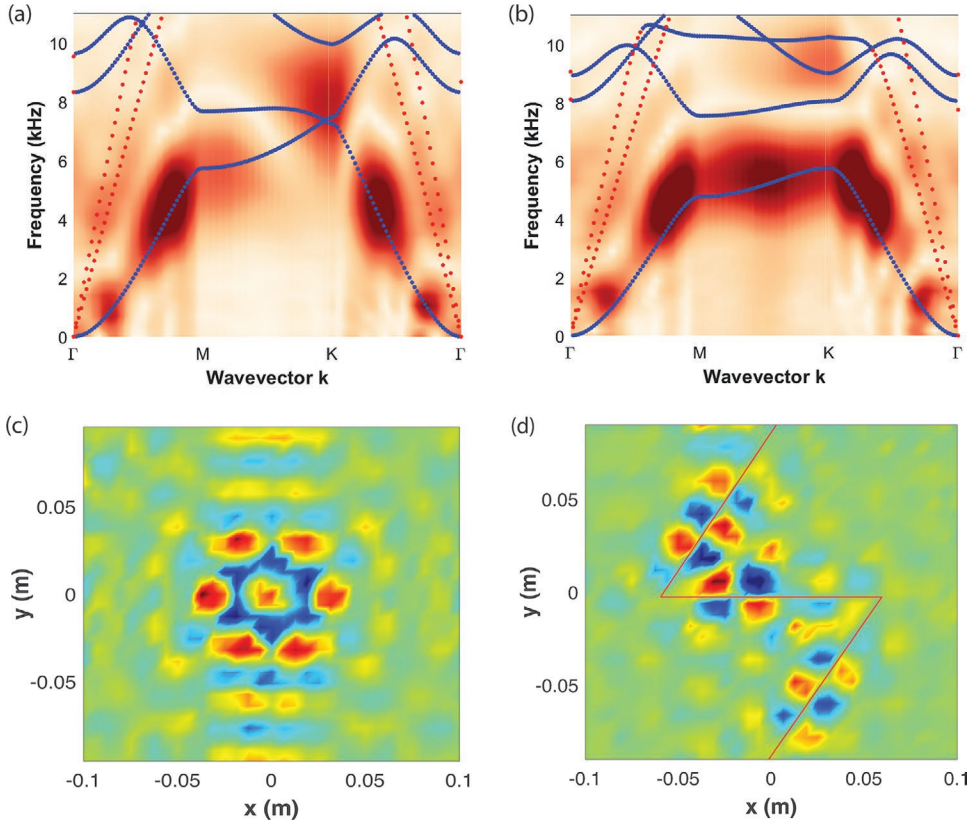

Figure 6. Experimental frequency/wavenumber representation along the reduced Brillouin zone (colormap) and comparison with numerical band structure predictions (dotted lines) for 2D hexagonal surfaces a) with $\gamma = 0$ and b) with $\gamma = 0.5$. The colormap corresponds to the magnitude of wavefields in reciprocal space obtained through 3D FT of experimental data (amplitude varies from white to red), while the blue and red dots respectively correspond to the numerical branches for out-of-plane and in-plane modes. c) Time snapshot of the experimental wavefield at 3.09 ms for the $\gamma = 0$ surface which shows evidence of the 6-fold symmetry. d) Time snapshot of the experimental wavefield in the presence of the zigzag interface for γvalues (±0.5) at 4.30 ms.

multifunctional performance[37] might be pursued by combining mechanical strength, with dynamic wave control and possibly acoustic functionalities.

5. Experimental Section

Sample Preparation: Geometries were generated in the MeshMixer software to construct 1D and 2D dimerized surfaces of assigned wall thickness. Fabrication of the 1D dimerized assembly was conducted by Formlabs Form 3 by Stereolithography. The lattice spacing was $2a$ = 15 mm and the printing material employed was durable resin of elastic modulus 1.0–1.5 GPa and density of 1130 kg m^{-3}. The overall dimension of the 1D specimen was 180.00 mm × 7.50 mm × 7.50 mm.

The 2D hexagonal surface materials were produced by Multi Jet Fusion, using HP Jet Fusion 4200 3D printer. All samples were built in Nylon 12 (HP 3D High Reusability PA 12), using a mixture of approximately 25% virgin powder and 75% recycled powder, as recommended by the manufacturer. As the material properties provided by the manufacturer refer to virgin powder,[38] the elastic properties of the printed material were measured by DMA and quasi-static tensile testing. The testing results, which are detailed in the Supporting Information, produce estimates for a Young's modulus of 1.5 GPa and for a Poisson's ratio of 0.4. A density of 1028 kg m^{-3} was measured with an Archimedes setup. These values were employed in the numerical simulations. The lattice spacing in the 2D hexagonal cell was 17.4 mm, and their overall finite size was 200.00 mm × 180.78 mm × 7.44 mm.

Numerical Simulations: The geometries employed for numerical simulations were first generated in Matlab and then processed in Meshmixer to produce the mesh file used for numerical discretization and 3D printing. All finite element simulations were performed using the "Shell module" of COMSOL Multiphysics. The polymer-based material (Young's modulus E = 1.77 GPa, Poisson's ratio ν = 0.35, density ρ = 1130 kg m^{-3}) was chosen as the elastic medium for the 1D dimerized waveguide, while Nylon-based material (Young's modulus E = 1.5 GPa, Poisson's ratio ν = 0.4, density ρ = 1028 kg m^{-3}) was the choice material for the 2D hexagonal surface materials. Based on eigenfrequency calculations, dispersion computations were performed by imposing Bloch periodic boundary conditions across the unit cells. The forced response computation was performed by considering a point load applying a force along the x_3 direction on the 2D hexagonal surface. The excitation point was located at the center of the upper surface. The average mesh sizes of the 1D dimerized and 2D hexagonal minimal surface-based materials were 0.338 and 0.578 mm, respectively.

Experimental Measurements: The vibration of the samples was generated by an electrodynamic shaker (Bruel & Kjaer V203) powered by a linear power amplifier (Bruel & Kjaer LDS LPA 100), and the out-of-plane velocities were detected optically by an SLDV (Polytec PSV-I-550) over a predefined grid of points. The 1D dimerized surface was mounted to the shaker at an off-center position relative to the interface in order to excite the flexural mode of interest efficiently, upon consideration that the mode of interest has a node right at the interface. Similarly, the shaker was attached to the center of the 2D hexagonal surface materials, and it was aligned with the transverse x_3 direction.

Supporting Information

Supporting Information is available from the Wiley Online Library or from the author.

Acknowledgements

Y.G., M.R., M.G., and M.R. acknowledge the support from the National Science Foundation (NSF) through the EFRI 1741685 grant and from the Army Research Office through grant W911NF-18-1-0036. B.D., B.F., and L.V. are grateful to Saratech Inc. for providing access to the HP4200 printer through the Saratech Center of Excellence in the Institute for Design and Manufacturing Innovation at UC Irvine.

Conflict of Interest

The authors declare no conflict of interest.

Data Availability Statement

The data that support the findings of this study are available from the corresponding author upon reasonable request.

Keywords

dimerized parameterization, elastic metamaterials, minimal surfaces, topological modes, valley states

Received: April 14, 2022
Published online:

[1] a) T. Tancogne-Dejean, M. Diamantopoulou, M. B. Gorji, C. Bonatti, D. Mohr, A. Mater, **2018**, *30*, 1803334; b) A. P. Kumar, T. Dirgantara, P. V. Krishna, *Advances in Lightweight Materials and Structures: Select Proceedings of ICALMS 2020*, Vol. *8*, Springer Nature, Singapore **2020**.
[2] X. Zheng, Z. Fu, K. Du, C. Wang, Y. Yi, *J. Mater. Sci.* **2018**, *53*, 10194.
[3] J. Bauer, L. R. Meza, T. A. Schaedler, R. Schwaiger, X. Zheng, L. Valdevit, *Adv. Mater.* **2017**, *29*, 1701850.
[4] S. C. Han, J. W. Lee, K. Kang, *Adv. Mater.* **2015**, *27*, 5506.
[5] J. Shi, H. Mofatteh, A. Mirabolghasemi, G. Desharnais, A. Akbarzadeh, *Adv. Mater.* **2021**, *33*, 2102423.
[6] S. J. Yeo, M. J. Oh, P. J. Yoo, *Adv. Mater.* **2019**, *31*, 1803670.
[7] A. H. Schoen, *Infinite periodic minimal surfaces without self-intersections*, National Aeronautics and Space Administration, USA **1970**.
[8] a) D. W. Abueidda, M. Bakir, R. K. A. Al-Rub, J. S. Bergström, N. A. Sobh, I. Jasiuk, *Mater. Des.* **2017**, *122*, 255; b) O. Al-Ketan, R. K. A. Al-Rub, R. Rowshan, *J. Mater. Res.* **2018**, *33*, 343; c) I. Maskery, L. Sturm, A. Aremu, A. Panesar, C. Williams, C. Tuck, R. D. Wildman, I. Ashcroft, R. J. Hague, *Polymer* **2018**, *152*, 62; d) M. Sychov, L. Lebedev, S. Dyachenko, L. Nefedova, *Acta Astronaut.* **2018**, *150*, 81; e) L. Yang, C. Yan, C. Han, P. Chen, S. Yang, Y. Shi, *Int. J. Mech. Sci.* **2018**, *148*, 149; f) L. Zhang, S. Feih, S. Daynes, S. Chang, M. Y. Wang, J. Wei, W. F. Lu, *Addit. Manuf.* **2018**, *23*, 505; g) Y. Zhang, M.-T. Hsieh, L. Valdevit, *Compos. Struct.* **2021**, *263*, 113693; h) M.-T. Hsieh, B. Endo, Y. Zhang, J. Bauer, L. Valdevit, *J. Mech. Phys. Solids* **2019**, *125*, 401; i) A. Guell Izard, J. Bauer, C. Crook, V. Turlo, L. Valdevit, *Small* **2019**, *15*, 1903834.
[9] S. C. Kapfer, S. T. Hyde, K. Mecke, C. H. Arns, G. E. Schröder-Turk, *Biomaterials* **2011**, *32*, 6875.
[10] O. Al-Ketan, R. K. Abu Al-Rub, *Adv. Eng. Mater.* **2019**, *21*, 1900524.
[11] Z. Wang, X. Wang, T. Gao, C. Shi, *Mech. Adv. Mater. Struct.* **2021**, *28*, 2057.
[12] M. Akbari, A. Mirabolghasemi, M. Bolhassani, A. Akbarzadeh, M. Akbarzadeh, *Adv. Funct. Mater.* **2022**, *32*, 2109725.
[13] M.-T. Hsieh, M. R. Begley, L. Valdevit, *Mater. Des.* **2021**, *207*, 109838.
[14] C. Y. Zhao, *Int. J. Heat Mass Transf.* **2012**, *55*, 3618.
[15] a) L. Han, S. Che, *Adv. Mater.* **2018**, *30*, 1705708; b) M. Fruchart, S.-Y. Jeon, K. Hur, V. Cheianov, U. Wiesner, V. Vitelli, *Proc. Natl. Acad. Sci. U. S. A.* **2018**, *115*, E3655; c) J. A. Dolan, B. D. Wilts, S. Vignolini, J. J. Baumberg, U. Steiner, T. D. Wilkinson, *Adv. Opt. Mater.* **2015**, *3*, 12.
[16] a) W. Wang, Y. Jin, W. Wang, B. Bonello, B. Djafari-Rouhani, R. Fleury, *Phys. Rev. B* **2020**, *101*, 024101; b) J. Vila, G. H. Paulino, M. Ruzzene, *Phys. Rev. B* **2019**, *99*, 125116.
[17] G. Ma, M. Xiao, C. T. Chan, *Nat. Rev. Phys.* **2019**, *1*, 281.
[18] a) P. Wang, L. Lu, K. Bertoldi, *Phys. Rev. Lett.* **2015**, *115*, 104302; b) Y.-T. Wang, P.-G. Luan, S. Zhang, *New J. Phys.* **2015**, *17*, 073031; c) N. P. Mitchell, L. M. Nash, W. T. M. Irvine, *Phys. Rev. B* **2018**, *98*, 174301.
[19] a) S. H. Mousavi, A. B. Khanikaev, Z. Wang, *Nat. Commun.* **2015**, *6*, 8682; b) M. Miniaci, R. Pal, B. Morvan, M. Ruzzene, *Phys. Rev. X* **2018**, *8*, 031074; c) S.-Y. Yu, C. He, Z. Wang, F.-K. Liu, X.-C. Sun, Z. Li, H.-Z. Lu, M.-H. Lu, X.-P. Liu, Y.-F. Chen, *Nat. Commun.* **2018**, *9*, 3072; d) Y. Guo, T. Dekorsy, M. Hettich, *Sci. Rep.* **2017**, *7*, 18043.
[20] R. K. Pal, M. Ruzzene, *New J. Phys.* **2017**, *19*, 025001.
[21] M. Yan, J. Lu, F. Li, W. Deng, X. Huang, J. Ma, Z. Liu, *Nat. Mater.* **2018**, *17*, 993.
[22] X.-T. He, E.-T. Liang, J.-J. Yuan, H.-Y. Qiu, X.-D. Chen, F.-L. Zhao, J.-W. Dong, *Nat. Commun.* **2019**, *10*, 872.
[23] M. Miniaci, R. K. Pal, R. Manna, M. Ruzzene, *Phys. Rev. B* **2019**, *100*, 024304.
[24] a) M. I. Rosa, Y. Guo, M. Ruzzene, *Appl. Phys. Lett.* **2021**, *118*, 131901; b) D. Beli, M. I. N. Rosa, C. De Marqui Jr, M. Ruzzene, *Extreme Mech. Lett.* **2021**, *44*, 101220.
[25] a) W. Deng, J. Lu, F. Li, X. Huang, M. Yan, J. Ma, Z. Liu, *Nat. Commun.* **2019**, *10*, 1769; b) M. Serra-Garcia, V. Peri, R. Süsstrunk, O. R. Bilal, T. Larsen, L. G. Villanueva, S. D. Huber, *Nature* **2018**, *555*, 342; c) Q. Wu, H. Chen, X. Li, G. Huang, *Phys. Rev. Appl.* **2020**, *14*, 014084; d) S. Li, D. Zhao, H. Niu, X. Zhu, J. Zang, *Nat. Commun.* **2018**, *9*, 1370; e) T.-W. Liu, F. Semperlotti, *Phys. Rev. Appl.* **2019**, *11*, 014040.
[26] J. Vila, R. K. Pal, M. Ruzzene, *Phys. Rev. B* **2017**, *96*, 134307.
[27] a) K. Qian, D. J. Apigo, C. Prodan, Y. Barlas, E. Prodan, *Phys. Rev. B* **2018**, *98*, 155138; b) H. Zhu, T.-W. Liu, F. Semperlotti, *Phys. Rev. B* **2018**, *97*, 174301; c) Q. Zhang, Y. Chen, K. Zhang, G. Hu, *Extreme Mech. Lett.* **2019**, *28*, 76.
[28] D. Anderson, H. Davis, J. Nitsche, L. Scriven, *Physics of Amphiphilic Layers* (Eds: J. Meunier, D. Langevin, N. Boccara), Vol. *21*, Springer, Berlin, Heidelberg **1987**, https://doi.org/10.1007/978-3-642-83202-4_17.
[29] M. Rossi, G. Buratti, *ShoCK!-Sharing Computational Knowledge!*, **2017**, pp. 259–268.
[30] M. Xiao, Z. Zhang, C. T. Chan, *Phys. Rev. X* **2014**, *4*, 021017.
[31] a) Y. Liu, X. Chen, Y. Xu, *Adv. Funct. Mater.* **2020**, *30*, 1904784; b) L. Li, Z. Xu, S. Chen, *Phys. Rev. B* **2014**, *89*, 085111.
[32] a) R. Chaunsali, E. Kim, A. Thakkar, P. G. Kevrekidis, J. Yang, *Phys. Rev. Lett.* **2017**, *119*, 024301; b) J. Yin, M. Ruzzene, J. Wen, D. Yu, L. Cai, L. Yue, *Sci. Rep.* **2018**, *8*, 6806.
[33] a) A. Srivastava, M. Sidler, A. V. Allain, D. S. Lembke, A. Kis, A. Imamoğlu, *Nat. Phys.* **2015**, *11*, 141; b) B. T. Zhou, K. Taguchi, Y. Kawaguchi, Y. Tanaka, K. T. Law, *Commun. Phys.* **2019**, *2*, 26.
[34] a) J. Zak, *Phys. Rev. B* **1985**, *32*, 2218; b) I. Kim, S. Iwamoto, Y. Arakawa, *Appl. Phys. Express* **2017**, *11*, 017201; c) M. Xiao, G. Ma, Z. Yang, P. Sheng, Z. Zhang, C. T. Chan, *Nat. Phys.* **2015**, *11*, 240.
[35] T. E. Michaels, J. E. Michaels, M. Ruzzene, *Ultrasonics* **2011**, *51*, 452.

[36] a) G.-H. Li, T.-X. Ma, Y.-Z. Wang, Y.-S. Wang, *Sci. Rep.* **2020**, *10*, 9376; b) L. Ning, Y.-Z. Wang, Y.-S. Wang, *Mech. Mater.* **2020**, *142*, 103300; c) L. Ning, Y.-Z. Wang, Y.-S. Wang, *Int. J. Solids Struct.* **2020**, *202*, 126.

[37] S. J. Callens, C. H. Arns, A. Kuliesh, A. A. Zadpoor, *Adv. Funct. Mater.* **2021**, *31*, 2101373.

[38] https://static1.sw-cdn.net/files/cms/materials/data-sheets/HP%20Data%20sheet.pdf (accessed: February 2022).